Consequences of large impacts on Enceladus' core shape

Julien Monteux, G. Collins, G. Tobie, Gael Choblet

To cite this version:

Julien Monteux, G. Collins, G. Tobie, Gael Choblet. Consequences of large impacts on Enceladus' core shape. Icarus, 2016, 264, pp.300 - 310. 10.1016/j.icarus.2015.09.034 . hal-01637425

HAL Id: hal-01637425
https://uca.hal.science/hal-01637425v1

Submitted on 16 Jan 2018

Consequences of large impacts on Enceladus' core shape

J. Monteux[a,b], G. S. Collins[c], G. Tobie[b], G. Choblet[b]

[a]*Laboratoire Magmas et Volcans, Université Blaise Pascal, CNRS, IRD, Clermont-Ferrand, France.*
[b]*Laboratoire de Planétologie et de Géodynamique de Nantes*
[c]*Impacts and Astromaterials Research Centre, Department of Earth Science and Engineering, Imperial College London.*

Abstract

The intense activity on Enceladus suggests a differentiated interior consisting of a rocky core, an internal ocean and an icy mantle. However, topography and gravity data suggests large heterogeneity in the interior, possibly including significant core topography. In the present study, we investigated the consequences of collisions with large impactors on the core shape. We performed impact simulations using the code iSALE2D considering large differentiated impactors with radius ranging between 25 and 100 km and impact velocities ranging between 0.24 to 2.4 km/s. Our simulations showed that the main controlling parameters for the post-impact shape of Enceladus' rock core are the impactor radius and velocity and to a lesser extent the presence of an internal water ocean and the porosity and strength of the rock core. For low energy impacts, the impactors do not pass completely through the icy mantle. Subsequent sinking and spreading of the impactor rock core lead to a positive core topographic anomaly. For moderately energetic impacts, the impactors completely penetrate through the icy mantle, inducing a negative core topography surrounded by a positive anomaly of smaller amplitude. The depth and lateral extent of the excavated area is mostly determined by the impactor radius and velocity. For highly energetic impacts, the rocky core is strongly deformed, and the full body is likely to be disrupted. Explaining the long-wavelength irregular shape of Enceladus' core by impacts would imply multiple low velocity (< 2.4 km/s) collisions with deca-kilometric differentiated impactors, which is possible only after the LHB period.

Keywords: Enceladus, Impact processes, Cratering, Interiors, Accretion

---

1. Introduction

Despite its small size ($R = 252$ km), Saturn's moon Enceladus is one of the most geologically active body of the Solar System. Its surprising endogenic activity is characterized by a very active province at the South Pole, from which eruptions of water vapor and ice grains emanating from warm tectonic ridges have been observed by the Cassini spacecraft (*Porco et al.*, 2006; *Hansen et al.*, 2006; *Waite et al.*, 2006; *Spencer et al.*, 2006). This activity is associated with a huge heat power estimated between 5 and 15 GW from thermal emission (*Spencer and Nimmo*, 2013), which implies a warm interior, consistent with a liquid water layer underneath the ice shell and a differentiated interior (*Nimmo et al.*, 2007; *Schubert et al.*, 2007). Models of tidal dissipation may explain why the activity is concentrated at the poles, where dissipation is predicted to be maximal (*Tobie et al.*, 2008; *B*e*hounková et al.*, 2010). However, there is still no satisfactory explanation for why this activity is located only in the south, and not in the north.

Based on the global shape data which show a depression at the south pole (*Thomas et al.*, 2007), it has been proposed that the ocean may be located only in the southern hemisphere (*Collins and Goodman*, 2007), thus explaining why the activity would be concentrated at the south (*Tobie et al.*, 2008). Gravity and shape data indicate that such an ocean would be at depths of about 30 to 40 kilometers and extend up to south latitudes of about 50°(*Iess et al.*, 2014). It has been proposed that the dichotomy between the north and south hemispheres may be the result of asymmetry in core shape (*McKinnon*, 2013). Due to the low pressure and moderate temperature expected in Enceladus' core, large topography anomalies may indeed be retained on very long periods of time (*McKinnon*, 2013) and may explain why convection-driven activities in the ice shell is confined only to the south polar terrain (*Showman et al.*, 2013). Besides the south polar depression, core topography anomalies could explain, at least partly, the existence of other big depressions observed at moderate latitudes (between 15°S and 50°N) and uncorrelated with any geological boundaries (*Schenk and McKinnon*, 2009).

McKinnon (2013) proposed three hypotheses to explain the possible irregularity of Enceladus' rocky core: accretional melting of the outer region of the icy moon associated with a degree-one instability; accretion of icy protomoons around irregular rock chunks; and collisional merger of two previously differentiated protomoons. Here we test the latter hypothesis by investigating the consequences of the collision of a large differentiated impactor on the shape of Enceladus' core. Collisions with large differentiated bodies were likely at the end of satellite accretion, during the final assemblage phase (e.g. *Asphaug and Reufer*, 2013). Large impact basins on other saturnian moons (e.g. Iapetus (*Giese et al.*, 2008), Mimas (*Schenk*, 2011), Titan (*Neish and Lorenz*, 2012)) and other solar system bodies (e.g. Vesta (*Schenk et al.*, 2012)) could represent remnant evidences of such collisions. Large impacts occurring at the end of the accretion and after, during the rest of the satellite's evolution, likely influenced the internal structure and especially the shape of its rocky core. It is also important to determine the conditions under which Enceladus would have survived disruption by collisions with deca-kilometric objects, which would place constraints on its accretion and the subsequent impact history.

To constrain the consequences of large-scale impacts on Enceladus, we simulated head-on collisions of differentiated impactors with diameter ranging between 50 and 200 km using the iSALE2D shock physics code (*Wünnemann et al.*, 2006; *Collins et al.*, 2004; *Davison et al.*, 2010). From these simulations, we tracked the evolution of rock fragments coming from the impactor and the impact-induced modification of Enceladus's core shape. In particular, we quantified the sensitivity in these outcomes to key model parameters, such as impactor velocity and radius, as well as structure and mechanical properties of Enceladus' interior (porosity, strength, temperature profile, core size, presence of an internal ocean). In section 2, we describe our numerical modelling approach; in section 3 we present our results. We discuss our results in the context of the presence of a water ocean in section 4. Conclusions are highlighted in section 5.

2. Impact modeling

To model the thermo-mechanical evolution of material during an impact between two differentiated icy bodies, we use iSALE2D (*Wünnemann et al.*, 2006; *Collins et al.*, 2004). This numerical model is a multi-rheology, multi-material shock physics code based on the SALE hydrocode (*Amsden et al.*, 1980) that has been extended and modified specifically to model planetary-scale impact crater formation (e.g., *Amsden et al.*, 1980; *Melosh et al.*, 1992; *Ivanov et al.*, 1997; *Collins et al.*, 2004; *Wünnemann et al.*, 2006; *Davison et al.*, 2010). In our simulations, the target structure and the impactor were simplified to two- or three- layer spherical bodies consisting of a rocky core, an icy mantle and for the three-layer case an internal ocean. Interpretation of gravity data collected by the Cassini spacecraft indicates that the core density could be as low as 2400 kg m^{-3}, corresponding to a core radius of about 200 km (*Iess et al.*, 2014). However, as Enceladus appears to be relatively far from hydrostatic equilibrium (*Iess et al.*, 2014), there are still significant uncertainties on the core radius and density. The low core density inferred from gravity data suggests that the rocky core might be significantly porous, with pores filled by water ice and/or liquid water, and that a significant fraction of the core may consist of hydrated silicate minerals. Currently, iSALE2D does not have provision to describe the behavior of an ice-rock or water-rock mixture. In our simulations, for simplicity, we assume complete segregation of the rock and ice-water phase into discrete layers and we consider dunite as representative of the rock phase (with density $\rho_s = 3330$ kg m^{-3}). We reduce the density of the core by including some initial porosity ϕ (defined as the ratio of pore volume to total volume) within it, varying from 0 to 50%, corresponding to radius varying between typically 160 km and 200 km. Assuming a core made of pure dunite, a radius as large as 200 km is consistent with a core porosity of about 50%, which is at the upper end of the estimated porosity in large asteroids (*Lindsay et al.*, 2015). A significant fraction of the core may also consist of hydrated minerals such as serpentine. In this case a 200 km core radius would imply a lower porosity. For simplicity, we consider only dunite as core materials and vary the porosity up to values of 50%. We also test the possible effect of porosity in the ice shell by considering values up to 20% as suggested by *Besserer et al.* (2013).

In our models, we consider the extreme case where the pores of both ice and rocks consist of voids, and are not filled with secondary materials (i.e. water or ice in rock pores). The difference between saturated porosity (with ice or liquid water) and voids may lead to differences in terms of mechanical and thermal properties. This aspect will be discussed in the last section. The effect of both rock and ice porosity is treated using the $\epsilon - \alpha$ porosity compaction model (*Wünnemann et al.*, 2006; *Collins et al.*, 2013), which accounts for the collapse of pore space by assuming that the compaction function depends upon volumetric strain. For sake of simplicity, we assume that the impactor material has an identical composition and porosity to those of the target.

The impact velocity v_{imp} can be decomposed into two contributions:

$$v_{imp} = \sqrt{v_{esc}^2 + v_\infty^2} \tag{1}$$

where v_{esc} is the escape velocity of the impacted planet and v_∞ is the velocity of the impactor at a distance much greater than that over which the gravitational attraction of the impacted planet is important. The escape velocity of Enceladus is $v_{esc} = 240$ m/s. As we consider collisions with relatively large objects ($R_{imp} = 25 - 100$ km), we limit our analysis to moderate relative velocities, varying between v_{esc} and $10 \times v_{esc}$, in order to limit the impact-induced deformation of the satellite and avoid full disruption (*Benz and Asphaug*, 1999; *Asphaug*, 2010). Moreover, this low-velocity impact regime is representative of the collisional environment at the end of the accretion. Indeed, N-body simulations from *Dwyer et al.* (2013) show that random impact velocity of proto-satellites mostly ranges between v_{esc} and $5v_{esc}$.

We approximated the thermodynamic response of the icy material using the Tillotson EoS for Ice as in *Bray et al.* (2008) and of the rocky material using the ANEOS EoS for dunite material as in *Benz et al.* (1989); *Davison et al.* (2010) (see Tab. 1 for parameter values). Standard strength parameters for dunite were used to form the static strength model for the rocky core (*Collins et al.*, 2004;

Davison et al., 2010). The static strength model for ice used in iSALE was derived from low temperature, high pressure laboratory data and accounts for the material strength dependence on pressure, damage and thermal softening (*Bray et al.*, 2008). We also explored the effect on our results of the cohesion of the damaged material (referred to here as Y_i for ice and Y_s rocks), which represents the minimum zero-pressure shear strength of cold material (strength is reduced to zero at the melt temperature). The minimum strength values considered in our models range between $10 - 500$ kPa for ice and $100 - 10^4$ kPa for silicate material. The Tillotson EoS for ice is severely limited in its applicability for hypervelocity impact; it includes no solid state or liquid phase changes. However, as we limit here our analysis to low velocity encounters ($240 < v_{imp} < 2400$ m s^{-1}), thought to be dominant at the end of the accretion, as shown in our simulations, no significant ice melting occurs and the use of Tillotson EoS is a reasonable approximation. We also used the Tillotson EoS for the liquid water.

Material weakening during impact may also be achieved by acoustic fluidization and/or thermal softening (*Melosh and Ivanov*, 1999), the latter of which is especially efficient for large-scale events (*Potter et al.*, 2012). Our simulations including acoustic fluidization that assumed typical block-model parameters favored in other works showed no significant effect on simulation results (see also discussion section). Hence, for simplicity and to reduce the number of free parameters, we chose to neglect acoustic fluidization. We do, however, include the effect of temperature on shear strength using the temperature-strength relationship proposed by *Ohnaka* (1995) and described by *Collins et al.* (2004) and we set the thermal softening coefficient in this expression to 1.2 as suggested by *Bray et al.* (2008). Since we consider the thermal softening during the impact, the thermal structure of Enceladus before the impact is probably a key parameter governing the post-impact state. However, the early temperature profile for such a small body is poorly constrained. Accretionary models seem to favour a cold accretion with inner temperatures close to the equilibrium temperature (*Schubert et al.*, 1981; *Monteux et al.*, 2014). To test the influence of the initial thermal conditions, we consider three different pre-impact temperature profiles for the impacted moon: constant temperature, conductive profile, two-layered advective profile. The impactor is assumed to have a constant temperature with $T = 100$ K.

Owing to the axisymmetric geometry of iSALE2D, we consider only head-on collisions (impact angle of 90° to the target tangent plane). The role of impact angle is left to future studies. To limit computation time, a 1-to-2 km spatial resolution is used, which is sufficient to describe the deflection of the rock core surface. The gravity is calculated from the density structure. For the largest and fastest impacts, we use iSALE2D's self-gravity gravity model (*Collins et al.*, 2011) to correctly assess the gravity field as the body is strongly deformed and the center of mass of the target moves upon the collision. As this self-gravity model is expensive in terms of computational time, we limit our post impact monitoring to the time needed to deform the rocky core (i.e. we consider that the fall-back of icy material and the icy-mantle slumping has only a very minor effect on the morphology of the rocky core). For all the impacts characterized here, this corresponds to the first hour after the impact.

3. Numerical results

3.1. Non-porous models

Fig. 1 shows three characteristic simulations: ($v_{imp} = 10v_{esc}$, $R_{imp} = 25$ km), ($v_{imp} = 10v_{esc}$, $R_{imp} = 75$ km) and ($v_{imp} = v_{esc}$, $R_{imp} = 75$ km). After such events, a large volume of Enceladus' mantle is displaced or escapes the orbit of the icy moon. To get a quantitative measure of deformation induced by the impact event, we monitor the plastic strain experienced by the impacted material. In particular, we calculate the total plastic strain which is the accumulated sum of plastic shear deformation, regardless of the sense of shear (*Collins et al.*, 2004). As represented in Fig. 1, the icy material is highly disturbed by the impact and most of the plastic deformation occurs in this layer. For the largest impact velocities (Fig. 1, left and middle), deformation also occurs at the top of the rocky core and leads to the formation of a depression. The material removed from the depression is displaced in a very small uplift of the core, surrounding the depression.

For small impact velocities (Fig. 1, right), the icy mantle is also highly deformed but the impactor's rocky core is trapped within the ice layer. In this low-velocity case, the deformation of the target's core and the impact melt production are minor but the surrounding ice is warmed up. Hence, over a longer time scale governed by a Stokes' flow, the impactor's core gently spreads over the surface of the pre-existing rocky core favoring the formation of successive fragmented silicate layers (*Roberts*, 2015). Depending on the impactor size and impact velocities, our simulations show that core merging occurs into three distinct regimes (Fig. 2):

(1) For small impactors and impact velocities close to $\sim v_{esc}$, the impactor's core is simply buried within Enceladus' icy mantle at a depth that scales with

the penetration depth p (*Orphal et al.*, 1980; *Murr et al.*, 1998) :

$$p/R_{imp} = Av_{imp}^{2/3} \tag{2}$$

where A is a function of the bulk sound velocity, the geometry and density difference between the impactor and the target.

(2) For higher impact velocities or larger impactors, the kinetic energy increases and hence penetration of the impactor's core through the target ice mantle is facilitated. When the impactor penetration depth, p (Eq.2), exceeds the ice-mantle thickness, δ_m, the impactor induces a deflection of the core boundary (Fig. 2), the amplitude of which depends on the impactor energy remaining after crossing the ice mantle. For $p \sim \delta_m$ or slightly larger, the impactor core spreads above the target's core (leading to a positive core-topography anomaly defined as the difference of post- and pre-impact core radii below the impact site). (3) However, if more energy is available, $p > \delta_m$ and the core is strongly deformed, possibly leading to severe deformation of the satellite, as illustrated in Fig. 2 for impactors larger than 75 km and/or impact velocities $\geq 10v_{esc}$. It has to be noted that, as we limit our post impact monitoring to one hour, for the most energetic impact cases with large impact velocities ($\geq$ 6 km/s) and large impactor radii ($\geq$ 75 km) the rocky material excavated from Enceladus' core and orbiting around the moon is still moving with significant velocity at the end of the simulation.

The thermal softening is an efficient process for large-scale events (*Potter et al.*, 2012). This process is strongly dependent on the pre-impact temperature field that is unfortunately poorly constrained. To test the influence of the pre-impact thermal state, we consider three different pre-impact temperature profiles for the impacted moon (Fig. 3): constant temperature (with

$T \sim 100K$), conductive profile (with a temperature gradient value of 1 K/km), two-layered convective profile (with a core temperature of 450 K and a mantle temperature of 250 K). As illustrated in Fig. 3, a hotter temperature profile in the icy shell strongly enhances the ice flow back and the refill of the core depression. One hour after the impact, a large cavity remains open in the icy mantle for the constant and cold temperature case. For the two-layered convective case where the mantle temperature is close to the melting temperature of ice, the icy mantle rapidly flows back leading to a huge jet of ice at the impact site. However, even if considering three pre-impact thermal states significantly modifies the post-impact dynamics of the icy mantle, this only weakly affects the depth of the depression within the rocky core that ranges between 12 an 15 km (Fig. 3). Hence, in the following, we consider models with a constant pre-impact temperature field.

3.2. Influence of ice and rock porosity

The porosity of the material involved during the impact is known to be a key factor in both the fragmentation and disruption of the impactor and the target (*Jutzi et al.*, 2008, 2009), and therefore it may play a role in our results. Enceladus is believed to contain a high degree of porosity, as are many other small bodies in the different populations of asteroids and comets (e.g. *Lindsay et al.*, 2015). To explain the long-wavelength topography of Enceladus, recent models also invoke porosity values ranging between 20 to 30 % within the icy mantle of Enceladus (*Besserer et al.*, 2013). We monitored the rocky core deformation as a function of the icy mantle porosity with porosities ranging between 0 and 20%. Similar to the simulations with different initial thermal conditions (Fig. 3), the dynamics of post-impact ice flow in the the deep cavity depends significantly on the porosity, as it affects the ice mechanical properties (Fig. 4). When the ice porosity equals 20% and because the compacted ice is thermally softened, the icy material (which is heated by impact to temperatures up to 250 K) re-fills the impact induced cavity in less than one hour.

Nevertheless, as illustrated in Fig. 5, the effect of the icy mantle porosity on the post-impact core morphology is rather small, at least for initial porosities ranging from 0 to 20% and for impact parameters leading to moderate core deformation ($v_{imp} = 10 v_{esc}$ and $R_{imp} = 25$ km). Fig. 6 shows the depth of the impact-induced core depression as a function of the mantle porosity. According to this figure, the depth of the depression ranges between 8 and 13 km. As mentioned earlier (see Fig. 4), the major influence of the mantle porosity is its ability to flow back and refill the core depression. As the impacted ice is severely deformed and compacted during the shockwave propagation, the impact will increase locally the porosity and the temperature of the icy mantle below the impact site.

Fig. 6 and Fig. 7 show that the influence of core porosity on core deformation is larger than the corresponding influence of mantle porosity. Indeed, increasing the porosity of the core from 0 to 50 % (and thus increasing its radius from 160 to 200) increases the maximum depth of the depression caused by the impact from $\sim$ 13 km to $\sim$ 31.5 km. To explain this feature, two effects shall be invoked. The first one is that increasing the rocky core porosity increases its size to maintain its mass. Hence, the top of the rocky core is closer to the surface and the impactor penetration depth needed to deform the rocky core is reduced accordingly. The second one is that porosity can enhance the rocky core deformation because the core material is less dense and easier to compact. To decipher between these two effects we ran a non-consistent model with a non-porous 200 km rocky core radius surrounded by a 50 km thick icy mantle

(Fig. 8, first column). At the end of this model, the depression depth is 18.5 km (compared to 31.5 km when the rocky core porosity is 50% and to 13 km when the rocky core has a radius of 160 km) meaning that both increasing the core size and the porosity favour deeper impact-induced depressions. This also suggests that density/compaction has a greater influence than core radius on the depth of the impact-induced core depression. We also ran a model with a 50% porosity 160 km rocky core radius (Fig. 6) where the obtained depression depth is 15 km (close to value obtained in the non-porous case). In this non-consistent case, a 8 km-thick ice block is trapped between the impactor and the target's core that prevents the formation of a deeper cavity. We should, however, keep in mind that in our simulations, we consider void porosity, while in reality pores should be filled by liquid water or water ice, which would affect compaction. The results presented here should be considered as an estimation of the maximal effect associated to impact-induced porosity compaction.

3.3. Influence of minimum strength values and water ocean

In all the models described above, the minimum strength values were set to $Y_i = 500$ kPa for ice and $Y_s = 10$ MPa for silicate material. These values represent the upper range of the plausible values since recent estimates of the strength of the surface of comet Tempel-1 obtained minima strength values in the order of 1-10 kPa (*Richardson and Melosh*, 2013). For the minimum strength of the rocky mantle, this value is also likely to range between the strength of the lunar soil (1 kPa) to the strength of the terrestrial soil ($<$ 100 kPa) (*Mitchell et al.*, 1972; *Lambe and Whitman*, 1979). We have tested the influence of these two parameters using lower values, $Y_i = 10$ kPa and $Y_s = 100$ kPa. As illustrated in Fig. 9 (second column) (called "highly deformable"), decreasing the minimum strength of both the ice and the rocky materials tends to increase the deformability of the rock core leading to both a deeper and wider depression. Ultimately, for a 200 km radius rocky core with 50% porosity (Fig. 9, second columns), the depth of the depression can reach 54.5 km. Here again, the conditions in term of porosity and strength are rather extreme, and the objectives of this simulation are to illustrate the maximal depression depth that could be generated by a large impact on Enceladus.

Fig. 8 (third and fourth columns) and 9 (third column) shows that the presence of a deep water ocean (considered as an inviscid fluid with a density of 910 kg/m^3) above the rocky core tends to reduce the impact-induced deflection of the core surface. Liquid water and water ice have comparable compressibility, water being slightly more compressible. The main difference concerns their resistance to shear. Liquid water has no strength (and is considered a completely inviscid material in the simulation), while ice has some strength. In the presence of liquid water, there is complete mechanical decoupling of shear deformation between the water and the core, whereas in the latter case shear stresses exist at the ice-core boundary. In the presence of the water ocean, the lateral extent of the morphology anomaly as well as its depth are smaller than without an ocean. Indeed, for $R_{core} = 160$ km, the depth of the impact induced cavity decreases from 13 km without an ocean to 3.5 km with an ocean. For $R_{core} = 200$ km and $\phi = 50\%$, the depth of the impact induced cavity decreases from 31.5 km without an ocean to 22.5 km with an ocean. This tends to illustrate that it is easier to enhance post-impact negative topography anomalies in the absence of a water ocean. Including a thick subsurface water ocean has the opposite effect of increasing the impact velocity or the impactor size, because it concentrates deformation in the ice mantle above, decoupling it from the rocky core below. On the other hand, the presence of the ocean seems to enhance the plastic strain in the deepest part of the core (Fig. 8, third and fourth columns). In parallel to compaction, impact-induced fracturing is likely to generate a porosity increase (via the dilatancy process) (*Collins*, 2014) that could in return favour fluid circulation within the deformed rocky core.

4. Discussion and Conclusion

In order to investigate the morphological consequences of collisions between differentiated impactors and Enceladus, we performed numerical impact simulations for impactor radii and velocities ranging between 10% to 40% Enceladus' radius and 1 to 10 times Enceladus' escape velocity (0.24 to 2.4 km/s), and for various assumptions for the structure and mechanical properties of Enceladus' interior. Our results showed that the dynamical response of the icy mantle to the impact is strongly dependent on the assumed thermo-mechanical properties for the ice. However, the icy mantle response has minor effects on the impact-induced deformation of the rock core. Only the presence of an internal ocean between the icy mantle and the rock core can significantly limit the rock core deformation.

Our simulations showed that the main controlling parameters for the post-impact shape of Enceladus' rock core are the impactor radius and velocity. We have identified three regimes: (1) For low energy impacts ($\leq 1.5 - 2 \times 10^{23}$ J), the impactors do not pass completely through the icy mantle and the core surface remains unmodified. The rock core of the impactors are deformed by the impact events, but remains trapped within the icy mantle. The impactor core embedded in the icy mantle would then progressively sink and spread, leading to a positive core topographic anomaly. (2) For more energetic impacts, the impactors completely penetrate though the icy mantle and hit the core surface. The impact leads to a negative core topography surrounded by a positive anomaly of smaller amplitude. The depth and lateral extent of the excavated area is mostly determined by the impactor radius and velocity. The shape of the excavated area can be significantly enhanced for high core porosity and very low material strengths, but its amplitude and extent remain primarily determined by the impactor parameters. In this regime, accounting for the acoustic fluidization does not change the final core morphology (not shown here). (3) For even more energetic impacts, the core is very strongly deformed, which does not appear to be compatible with Enceladus' core morphology (see Fig. 2). Our simulations of these events do not follow the full evolution of the impact scenario so we cannot predict the final core structure; however, it is likely that some of these events lead to full body disruption and that, in non-disruptive impacts, acoustic fluidization may contribute to the final shape of the rocky core and would therefore need to be included to analyze possible outcomes.

For impact velocities higher than 2.4 km.s^{-1}($10 \times v_{esc}$), moderate deformation of the core is possible only for impactors smaller than 25 km. During the Late Heavy Bombardment, high-velocity collisions with impactors exceeding 20 km is likely and therefore, as recently highlighted by *Movshovitz et al.* (2015), full disruption and re-accretion of the satellite may have occurred possibly several times during this period. This implies that any large impact leaving a long-wavelength signature on the core shape should have taken place after the Late Heavy Bombardement. This also requires relatively low velocity impacts, and therefore encounter with planetocentric bodies rather than with heliocentric bodies. Alternatively, as proposed by *Charnoz et al.* (2011), Enceladus may have formed late during the history of the Saturn system, thus limiting the risk of full disruption. Following the model of *Charnoz et al.* (2011), Enceladus may have accreted from a swarm of differentiated embryos emerging from the outer edge of a massive ring system. In such a model, multiple low velocity collisions between decametric differentiated impactors and a growing Enceladus are expected. The irregular core shape of Enceladus, as constrained from Cassini gravity and topography data (*McKinnon*, 2013; *Lefèvre et al.*, 2015), may constitute a record of this accretional process.

Various processes will probably alter the core topography after an impact event, so that the amplitude of core deflection predicted in our simulations should be considered as an upper limit. Rock fragments would be likely transported by the ice flow back to the impact cavity, filling partly the impact-induced depression. Even if the core is relatively cold, topography relaxation may occur to some extent, especially for low-strength rock material. Prolonged water interactions may also partly erode the topography and again reduce the topography anomaly. Detailed modelling of the subsequent topography evolution is beyond the scope of the present study, and will require future modeling effort. The 2D nature of our simulations also optimizes the amplitude of impact-induced core deflection as only head-on collisions can be considered. It is known that impact angle affects the strength and distribution of the shock wave generated in the impact and therefore the perturbed region (e.g. *Pierazzo and Melosh*, 2000). For more oblique impacts, the impactor kinetic energy will be more efficiently transferred to the icy mantle, leading to a more efficient deformation of the icy mantle and a larger amount of escaping materials (e.g. *Korycansky and Zahnle*, 2011). The volume of icy mantle affected by the impact, which is already large for head-on collisions as shown with our 2D simulations, will be further increased. Another limitation of our modelling approach is the assumption regarding the mechanical properties of the rock core. We considered dunite with various degree of void porosity as representative of the rock core composition, since a relatively well-defined equation of state exists for this material (*Davison et al.*, 2010). Based on the interpretation of the Cassini gravity data, which suggest a low density core (2400 kg.m^{-3}, *Iess et al.* (2014)), the rock core may contain a significant fraction of highly hydrated minerals, as well as free water or/and ice in rock pores. Currently, we are not able to consider a mixture of ice and rocks for both the impactor's core and the target's core. However, to estimate an upper limit of the deformation, we have performed a run corresponding to our classical impact model ($v_{imp} = 10v_{esc}$ and $R_{imp} = 25$ km) with 100% ice-filled pores (i.e. a core made of pure ice). In this unrealistic case (not shown here), the impactor's core is eventually buried at a depth of $\sim$ 170 km (i.e. 80 km below the core-mantle boundary) which is far larger than the depth of the depression ($\sim$ 30 km) obtained with a 50% porous rocky core. This limitation also stands for the structure of the impactor's core that is likely to have remained undifferentiated in the context of an early formation. To estimate the influence of the impactor's degree of differentiation, we have also considered the $v_{imp} = 10v_{esc}$ case with a 25 km radius impactor made of pure ice and an impactor made of pure dunite. In the first case, the impact induces a flattening of $\sim$ 0.4 km at the core's surface below the impact site (see Fig. 6). In the second case, the impact induces a flattening of $\sim$ 23.2 km. This result, even if performed for an unrealistic water ice content, suggests the ice/rock ratio in the core may play a strong influence on the response of the core to large impacts. This suggests that the results presented here should be considered valid only for differentiated interior models with rock-dominated core and a relatively small porosity content (<10-20%). Future works are required constrain more precisely the effect of hydrated minerals and mixture with high ice-water/rock ratio in the interior.

Large impacts are likely to modify the ice/rock ratio by eroding significantly the shallower part of the impacted moon. Our results show that vertical impacts with $v_{imp} > 6v_{esc}$ and $R_{imp} > 75$ km, can erode up to half the ice volume from the impacted body (Fig. 1, second column). Several factors such as a hot, porous pre-impact mantle and the presence of a deep water ocean increase the ability of the icy mantle to deform. Hence, these parameters are also likely to influence the post-impact ice/rock ratio by decreasing the fraction of ice in the post-impact moon. The impact angle is another key parameter that governs the fraction of escaped material (e.g. *Korycansky and Zahnle*, 2011). However, to limit the computational time and as we have restricted our study to vertical impacts, monitoring the long-term evolution of the ice/rock ratio is beyond the scope of our study.

Despite the limitations, the simulations we performed highlight the crucial role played by impacts on the evolution of Enceladus. Besides explaining the irregular shape of the core, impacts also provide efficient mechanisms to enhance thermo-chemical exchanges between the deep interior and the surface. For models with an internal water ocean, we can see that a large volume of the ocean is temporarily exposed to the surface, thus potentially releasing a large fraction of volatile initially stored dissolved in the ocean. Large impacts cause a strong damage of the ice on a very large portion of the icy mantle, which will likely have consequences on the subsequent convective mantle dynamics and interaction with the fractured surface. These also lead to a large plastic strain in the rock core underneath the impact site, which may enhance macroporosity. This would promote fluid circulation throughout a large fraction of the core, favoring serpentinization processes (*Malamud and Prialnik*, 2013) and hydrothermal activities (e.g. *Hsu et al.*, 2015). Further modeling efforts will be needed to understand the consequences of such impact events on the long-term evolution of Enceladus. Lastly, the effects of large impacts are not confined to Enceladus. Similar effects are very likely on the other moons of Saturn as well as on other planetary objects, such as Ceres (*Davison et al.*, 2015; *Ivanov*, 2015, e.g.) and Pluto (*Bray and Schenk*, 2015, e.g.) for which impact bombardment has probably played a key role in their evolution.

Acknowledgements

J. Monteux was funded by Agence Nationale de la Recherche (Accretis decision no. ANR-10-PDOC-001-01). The research leading to these results has received funding from the European Research Council under the European Community's Seventh Framework Programme (FP7/2007- 2013 Grant Agreement no. 259285). We gratefully acknowledge the developers of iSALE, including Kai Wünnemann, Boris Ivanov, Jay Melosh, and Dirk Elbeshausen. We also thank Katarina Miljkovich and Tom Davison for useful discussions.

Amsden, A. A., H. M. Ruppel, and C. W. Hirt (1980), SALE: Simplified ALE Computer Program for Fluid Flow at All Speeds, *Tech. Rep. LA-8095*, *Los Alamos Natl. Lab., Los Alamos, N. M.*

Asphaug, E. (2010), Similar-sized collisions and the diversity of planets, *Chemie der Erde / Geochemistry*, *70*, 199–219, doi:10.1016/j.chemer.2010.01.004.

Asphaug, E., and A. Reufer (2013), Late origin of the Saturn system, *Icarus*, *223*, 544–565, doi:10.1016/j.icarus.2012.12.009.

Benz, W., and E. Asphaug (1999), Catastrophic Disruptions Revisited, *Icarus*, *142*, 5–20, doi:10.1006/icar.1999.6204.

Benz, W., A. G. W. Cameron, and H. J. Melosh (1989), The origin of the moon and the single impact hypothesis. III, *Icarus*, *81*, 113–131, doi:10.1016/0019-1035(89)90129-2.

Besserer, J., F. Nimmo, J. H. Roberts, and R. T. Pappalardo (2013), Convection-driven compaction as a possible origin of Enceladus's long wavelength topography, *Journal of Geophysical Research (Planets)*, *118*, 908–915, doi:10.1002/jgre.20079.

Bray, V. J., and P. M. Schenk (2015), Pristine impact crater morphology on Pluto - Expectations for New Horizons, *Icarus*, *246*, 156–164, doi:10.1016/j.icarus.2014.05.005.

Bray, V. J., G. S. Collins, J. V. Morgan, and P. M. Schenk (2008), The effect of target properties on crater morphology: Comparison of central peak craters on the Moon and Ganymede, *Meteoritics and Planetary Science*, *43*, 1979–1992, doi:10.1111/j.1945-5100.2008.tb00656.x.

B**e**hounková, M., G. Tobie, G. Choblet, and O. **C**adek (2010), Coupling mantle convection and tidal dissipation: Applications to Enceladus and Earth-like planets, *Journal of Geophysical Research (Planets)*, *115*, E09011, doi:10.1029/2009JE003564.

Charnoz, S., A. Crida, J. C. Castillo-Rogez, V. Lainey, L. Dones, Ö. Karatekin, G. Tobie, S. Mathis, C. Le Poncin-Lafitte, and J. Salmon (2011), Accretion of Saturn's mid-sized moons during the viscous spreading of young massive rings: Solving the paradox of silicate-poor rings versus silicate-rich moons, *Icarus*, *216*, 535–550, doi:10.1016/j.icarus.2011.09.017.

Collins, G. C., and J. C. Goodman (2007), Enceladus' south polar sea, *Icarus*, *189*, 72–82, doi:10.1016/j.icarus.2007.01.010.

Collins, G. S. (2014), Numerical simulations of impact crater formation with dilatancy, *J. Geophys. Res. Planets*, *119*, 1–20, doi:10.1002/2014JE004708.

Collins, G. S., H. J. Melosh, and B. A. Ivanov (2004), Modeling damage and deformation in impact simulations, *Meteoritics and Planetary Science*, *39*, 217–231, doi:10.1111/j.1945-5100.2004.tb00337.x.

Collins, G. S., T. M. Davison, and F. J. Ciesla (2011), Numerical Simulations of Sub-Catastrophic Porous Planetesimal Collisions, in *Lunar and Planetary Science Conference*, *Lunar and Planetary Science Conference*, vol. 42, p. 1933.

Collins, G. S., H. J. Melosh, and K. Wünnemann (2013), Improvements to the $\epsilon - \alpha$ Porous Compaction Model for Simulating Impacts into High-Porosity Solar System Objects, *Int. J. Impact Eng.*, *38*, 434–439.

Davison, T. M., G. S. Collins, and F. J. Ciesla (2010), Numerical modelling of heating in porous planetesimal collisions, *Icarus*, *208*, 468–481, doi:10.1016/j.icarus.2010.01.034.

Davison, T. M., G. S. Collins, D. P. O'Brien, F. J. Ciesla, P. A. Bland, and B. J. Travis (2015), Impact Bombardment of Ceres, in *Lunar and Planetary Science Conference*, *Lunar and Planetary Science Conference*, vol. 46, p. 2116.

Dwyer, C. A., F. Nimmo, M. Ogihara, and S. Ida (2013), The influence of imperfect accretion and radial mixing on ice:rock ratios in the Galilean satellites, *Icarus*, *225*, 390–402, doi:10.1016/j.icarus.2013.03.025.

Giese, B., R. Wagner, H. Hussmann, G. Neukum, J. Perry, P. Helfenstein, and P. C. Thomas (2008), Enceladus: An estimate of heat flux and lithospheric thickness from flexurally supported topography, *Geophys. Res. Lett.*, *35*, L24204, doi:10.1029/2008GL036149.

Hansen, C. J., L. Esposito, A. I. F. Stewart, J. Colwell, A. Hendrix, W. Pryor, D. Shemansky, and R. West (2006), Enceladus' Water Vapor Plume, *Science*, *311*, 1422–1425, doi:10.1126/science.1121254.

Hsu, H.-W., F. Postberg, Y. Sekine, T. Shibuya, S. Kempf, M. Horányi, A. Juhász, N. Altobelli, K. Suzuki, Y. Masaki, T. Kuwatani, S. Tachibana, S.-I. Sirono, G. Moragas-Klostermeyer, and R. Srama (2015), Ongoing hydrothermal activities within Enceladus, *Nature*, *519*, 207–210, doi:10.1038/nature14262.

Iess, L., D. J. Stevenson, M. Parisi, D. Hemingway, R. A. Jacobson, J. I. Lunine, F. Nimmo, J. W. Armstrong, S. W. Asmar, M. Ducci, and P. Tortora (2014), The Gravity Field and Interior Structure of Enceladus, *Science*, *344*, 78–80, doi:10.1126/science.1250551.

Ivanov, B. A. (2015), Ceres: Possible Records of Giant Impacts, in *Lunar and Planetary Science Conference*, *Lunar and Planetary Science Conference*, vol. 46, p. 1077.

Ivanov, B. A., D. Deniem, and G. Neukum (1997), Implementation of Dynamic Strength Models into 2D Hydrocodes: Applications for Atmospheric Breakup and Impact Cratering, *Int. J. Impact Eng.*, *20*, 411–430.

Jutzi, M., W. Benz, and P. Michel (2008), Numerical simulations of impacts involving porous bodies. I. Implementing sub-resolution porosity in a 3D SPH hydrocode, *Icarus*, *198*, 242–255, doi:10.1016/j.icarus.2008.06.013.

Jutzi, M., P. Michel, K. Hiraoka, A. M. Nakamura, and W. Benz (2009), Numerical simulations of impacts involving porous bodies. II. Comparison with laboratory experiments, *Icarus*, *201*, 802–813, doi:10.1016/j.icarus.2009.01.018.

Korycansky, D. G., and K. J. Zahnle (2011), Titan impacts and escape, *Icarus*, *211*, 707–721, doi:10.1016/j.icarus.2010.09.013.

Lambe, T., and R. Whitman (1979), *Soil mechanics, SI version*, Series in soil engineering, Wiley.

Lefèvre, A., G. Tobie, G. Choblet, O. Cadek, G. Mitri, M. Massé, and M. Behounkova (2015), Enceladus' internal ocean constrained from Cassini gravity and topography data, in *European Planetary Science Conference*.

Lindsay, S. S., F. Marchis, J. P. Emery, J. E. Enriquez, and M. Assafin (2015), Composition, mineralogy, and porosity of multiple asteroid systems from visible and near-infrared spectral data, *Icarus*, *247*, 53–70, doi:10.1016/j.icarus.2014.08.040.

Malamud, U., and D. Prialnik (2013), Modeling serpentinization: Applied to the early evolution of Enceladus and Mimas, *Icarus*, *225*, 763–774, doi:10.1016/j.icarus.2013.04.024.

McKinnon, W. B. (2013), The shape of Enceladus as explained by an irregular core: Implications for gravity, libration, and survival of its subsurface ocean, *Journal of Geophysical Research (Planets)*, *118*, 1775–1788, doi:10.1002/jgre.20122.

Melosh, H. J., and B. A. Ivanov (1999), Impact Crater Collapse, *Annual Review of Earth and Planetary Sciences*, *27*, 385–415, doi:10.1146/annurev.earth.27.1.385.

Melosh, H. J., E. V. Ryan, and E. Asphaug (1992), Dynamic fragmentation in impacts - Hydrocode simulation of laboratory impacts, *J. Geophys. Res.*, *97*, 14,735, doi:10.1029/92JE01632.

Mitchell, J. K., W. N. Houston, R. F. Scott, N. C. Costes, W. D. Carrier, III, and L. G. Bromwell (1972), Mechanical properties of lunar soil: Density, porosity, cohesion and angle of internal friction, in *Lunar and Planetary Science Conference Proceedings*, *Lunar and Planetary Science Conference Proceedings*, vol. 3, edited by A. E. Metzger, J. I. Trombka, L. E. Peterson, R. C. Reedy, and J. R. Arnold, p. 3235.

Monteux, J., G. Tobie, G. Choblet, and M. Le Feuvre (2014), Can large icy moons accrete undifferentiated?, *Icarus*, *237*, 377–387, doi: 10.1016/j.icarus.2014.04.041.

Movshovitz, N., F. Nimmo, D. G. Korycansky, E. Asphaug, and J. M. Owen (2015), Disruption and reaccretion of midsized moons during an outer solar system Late Heavy Bombardment, *Geophys. Res. Lett.*, *42*, 256–263, doi: 10.1002/2014GL062133.

Murr, L., S. A. Quinones, E. F. T, A. Ayala, O. L. Valerio, F. Horz, and R. Bernhard (1998), The low-velocity-to-hypervelocity penetration transition for impact craters in metal targets, *Materials Science and Engineering*, *256*, 166–182.

Neish, C. D., and R. D. Lorenz (2012), Titan's global crater population: A new assessment, *Planet. Space Sci.*, *60*, 26–33, doi:10.1016/j.pss.2011.02.016.

Nimmo, F., J. R. Spencer, R. T. Pappalardo, and M. E. Mullen (2007), Shear heating as the origin of the plumes and heat flux on Enceladus, *Nature*, *447*, 289–291, doi:10.1038/nature05783.

Ohnaka, M. (1995), A shear failure strength law of rock in the brittle-plastic transition regime, *Geophys. Res. Lett.*, *22*, 25–28, doi:10.1029/94GL02791.

Orphal, D. L., W. F. Borden, S. A. Larson, and P. H. Schultz (1980), Impact melt generation and transport, in *Lunar and Planetary Science Conference Proceedings*, *Lunar and Planetary Science Conference Proceedings*, vol. 11, edited by S. A. Bedini, pp. 2309–2323.

Pierazzo, E., and H. J. Melosh (2000), Melt Production in Oblique Impacts, *Icarus*, *145*, 252–261, doi:10.1006/icar.1999.6332.

Porco, C. C., P. Helfenstein, P. C. Thomas, A. P. Ingersoll, J. Wisdom, R. West, G. Neukum, T. Denk, R. Wagner, T. Roatsch, S. Kieffer, E. Turtle, A. McEwen, T. V. Johnson, J. Rathbun, J. Veverka, D. Wilson, J. Perry, J. Spitale, A. Brahic, J. A. Burns, A. D. Del Genio, L. Dones, C. D. Murray, and S. Squyres (2006), Cassini Observes the Active South Pole of Enceladus, *Science*, *311*, 1393–1401, doi:10.1126/science.1123013.

Potter, R. W. K., G. S. Collins, W. S. Kiefer, P. J. McGovern, and D. A. Kring (2012), Constraining the size of the South Pole-Aitken basin impact, *Icarus*, *220*, 730–743, doi:10.1016/j.icarus.2012.05.032.

Richardson, J. E., and J. H. Melosh (2013), An examination of the Deep Impact collision site on Comet Tempel 1 via Stardust-NExT: Placing further constraints on cometary surface properties, *Icarus*, *222*, 492–501, doi:10.1016/j.icarus.2012.04.019.

Roberts, J. H. (2015), The fluffy core of Enceladus, *Icarus*, *258*, 54–66, doi:10.1016/j.icarus.2015.05.033.

Schenk, P. (2011), Geology of Mimas?, in *Lunar and Planetary Science Conference*, *Lunar and Planetary Inst. Technical Report*, vol. 42, p. 2729.

Schenk, P., D. P. O'Brien, S. Marchi, R. Gaskell, F. Preusker, T. Roatsch, R. Jaumann, D. Buczkowski, T. McCord, H. Y. McSween, D. Williams,

A. Yingst, C. Raymond, and C. Russell (2012), The Geologically Recent Giant Impact Basins at Vesta South Pole, *Science*, *336*, 694–, doi: 10.1126/science.1223272.

Schenk, P. M., and W. B. McKinnon (2009), One-hundred-km-scale basins on Enceladus: Evidence for an active ice shell, *Geophys. Res. Lett.*, *36*, L16202, doi:10.1029/2009GL039916.

Schubert, G., D. J. Stevenson, and K. Ellsworth (1981), Internal structures of the Galilean satellites, *Icarus*, *47*, 46–59, doi:10.1016/0019-1035(81)90090-7.

Schubert, G., J. D. Anderson, B. J. Travis, and J. Palguta (2007), Enceladus: Present internal structure and differentiation by early and long-term radiogenic heating, *Icarus*, *188*, 345–355, doi:10.1016/j.icarus.2006.12.012.

Showman, A. P., L. Han, and W. B. Hubbard (2013), The effect of an asymmetric core on convection in Enceladus' ice shell: Implications for south polar tectonics and heat flux, *Geophys. Res. Lett.*, *40*, 5610–5614, doi: 10.1002/2013GL057149.

Spencer, J. R., and F. Nimmo (2013), Enceladus: An Active Ice World in the Saturn System, *Annual Review of Earth and Planetary Sciences*, *41*, 693–717, doi:10.1146/annurev-earth-050212-124025.

Spencer, J. R., J. C. Pearl, M. Segura, F. M. Flasar, A. Mamoutkine, P. Romani, B. J. Buratti, A. R. Hendrix, L. J. Spilker, and R. M. C. Lopes (2006), Cassini Encounters Enceladus: Background and the Discovery of a South Polar Hot Spot, *Science*, *311*, 1401–1405, doi:10.1126/science.1121661.

Thomas, P. C., J. A. Burns, P. Helfenstein, S. Squyres, J. Veverka, C. Porco, E. P. Turtle, A. McEwen, T. Denk, B. Giese, T. Roatsch, T. V. Johnson, and R. A. Jacobson (2007), Shapes of the saturnian icy satellites and their significance, *Icarus*, *190*, 573–584, doi:10.1016/j.icarus.2007.03.012.

Tobie, G., O. **C**adek, and C. Sotin (2008), Solid tidal friction above a liquid water reservoir as the origin of the south pole hotspot on Enceladus, *Icarus*, *196*, 642–652, doi:10.1016/j.icarus.2008.03.008.

Waite, J. H., M. R. Combi, W.-H. Ip, T. E. Cravens, R. L. McNutt, W. Kasprzak, R. Yelle, J. Luhmann, H. Niemann, D. Gell, B. Magee, G. Fletcher, J. Lunine, and W.-L. Tseng (2006), Cassini Ion and Neutral Mass Spectrometer: Enceladus Plume Composition and Structure, *Science*, *311*, 1419–1422, doi:10.1126/science.1121290.

Wünnemann, K., G. S. Collins, and H. J. Melosh (2006), A strain-based porosity model for use in hydrocode simulations of impacts and implications for transient crater growth in porous targets, *Icarus*, *180*, 514–527, doi:10.1016/j.icarus.2005.10.013.

Table 1: Typical parameter values for numerical models

Enceladus radius	R	250 km
Rocky core radius	R_{core}	160-200 km
Icy mantle thickness	δ_m	50-90 km
Surface gravity field	g_0	0.113 m.s $^{-2}$
Escape velocity	v_{esc}	240 m/s
Impactor radius	R_{imp}	25-100 km
Impact velocity	v_{imp}	240-2400 m/s
Mantle properties (Ice)		
Initial density	ρ_i	820 kg.m^{-3}
Equation of state type		Tillotson
Poisson		0.33
Porosity		0-20%
Minimum strength	Y_i	10-500 kPa
Core properties (Dunite)		
Rocky core density	ρ_s	3330 kg.m^{-3}
Equation of state type		ANEOS
Poisson		0.25
Porosity		0-50%
Minimum strength	Y_s	100 kPa-10 MPa

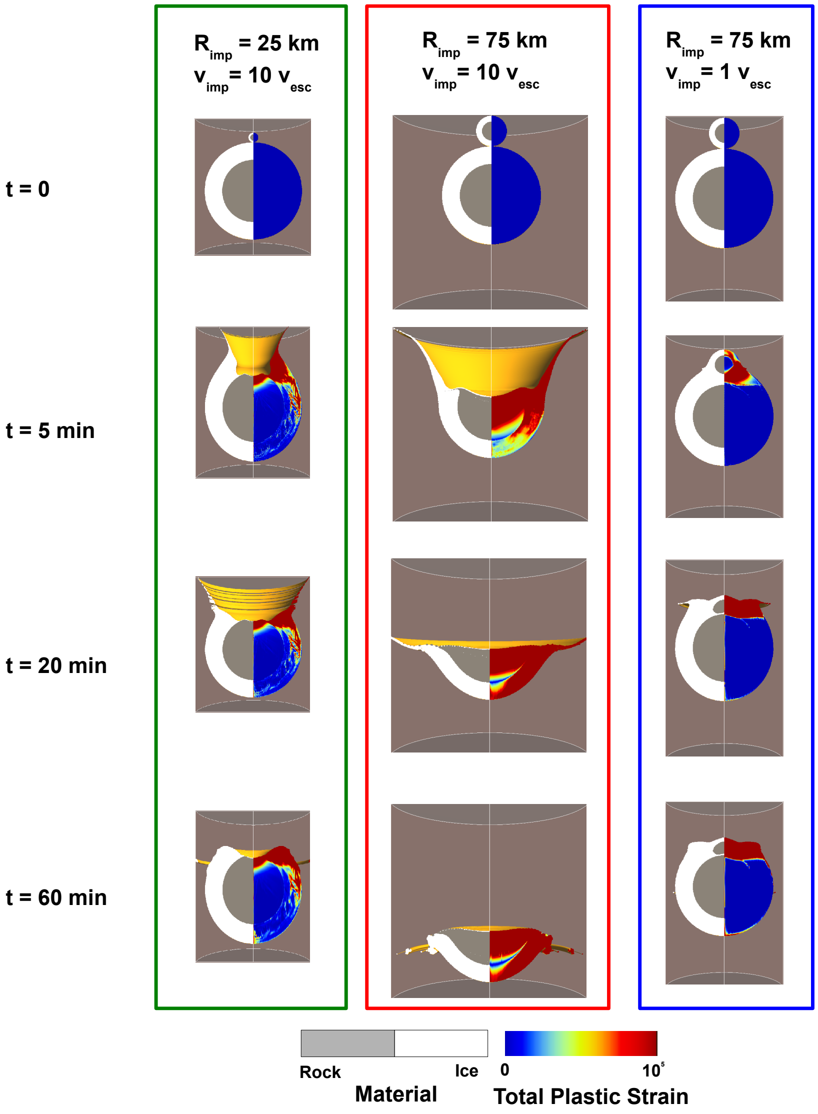

Figure 1: Material repartition (left column) and total plastic deformation (right column) as a function of time (from top to bottom) on Enceladus for 3 impact cases: ($v_{imp} = 10v_{esc}$, $R_{imp} = 25$ km) (left), ($v_{imp} = 10v_{esc}$, $R_{imp} = 75$ km) (centre) and ($v_{imp} = v_{esc}$, $R_{imp} = 75$ km) (right). In these models, the grid resolution is 1 km in all directions. Here both the rocky core and the icy material are considered as nonporous materials.

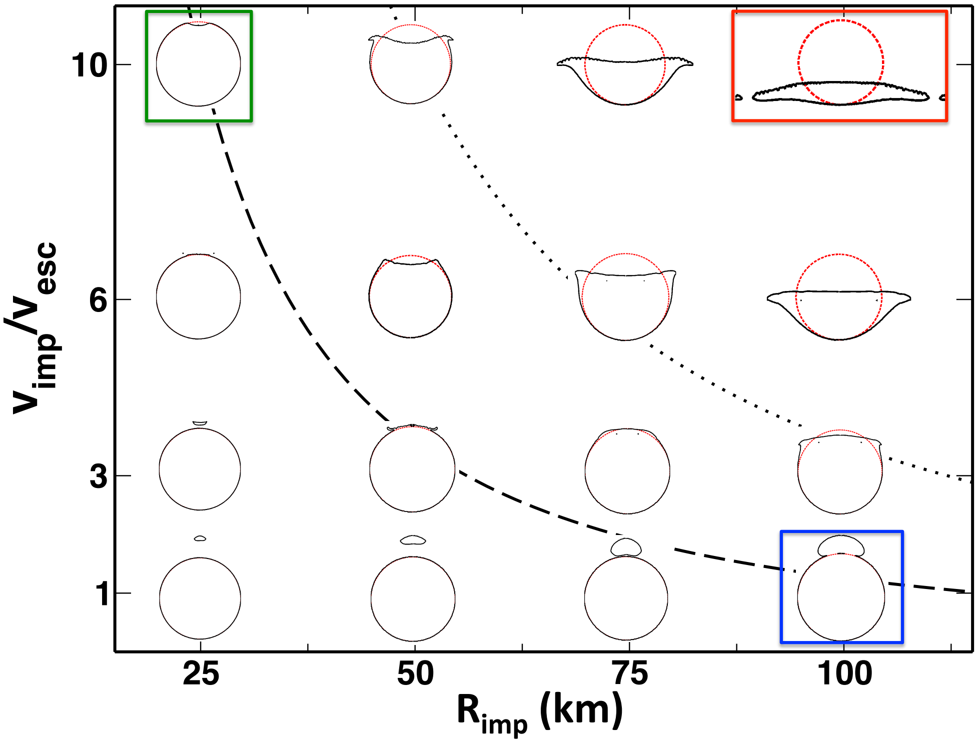

Figure 2: Rocky core morphology as a function of the impactor size and the impact velocity ($v_{esc} = 240$ m/s). In these models the porosity of the icy material is zero. For each morphology, the red circle represents the pre-impact spherical shape of the impacted core. The dashed black line represents Eq.2 with $A = 2$. Above this critical theoretical line, the impact induced topography is negative. Below this critical theoretical line, the impact induced topography is positive. The dotted black line represents Eq.2 with $A = 1$. Above this critical theoretical line, very highly deformed cores are formed and acoustic fluidization may contribute to their final shape. However the deformation is too large and probably not compatible with the Enceladus morphology. We limit our post impact monitoring to one hour which means that for large impact velocities (≥ 6 km/s) and large impactor radii (≥ 75 km) the rocky material excavated from Enceladus' core and orbiting around the moon is still moving with significant velocity at the end of the simulation.

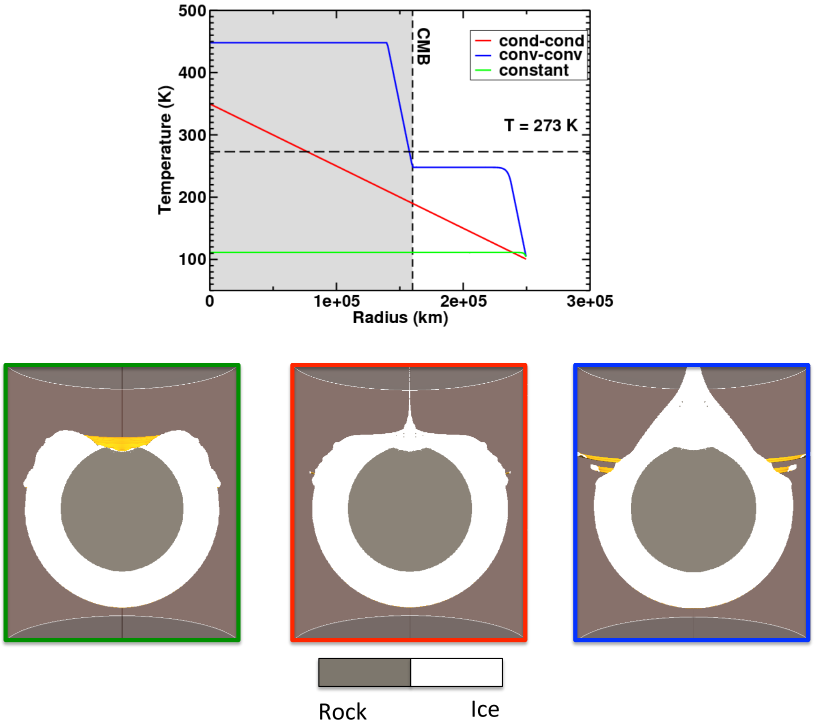

Figure 3: Material repartition one hour after the impact (bottom) for three different pre-impact temperature profiles (top) (with $v_{imp} = 10v_{esc}$, $R_{core} = 160$ km and $R_{imp} = 25$ km). The color of the temperature profile corresponds to the color of the rectangle surrounding the material repartition snapshot.

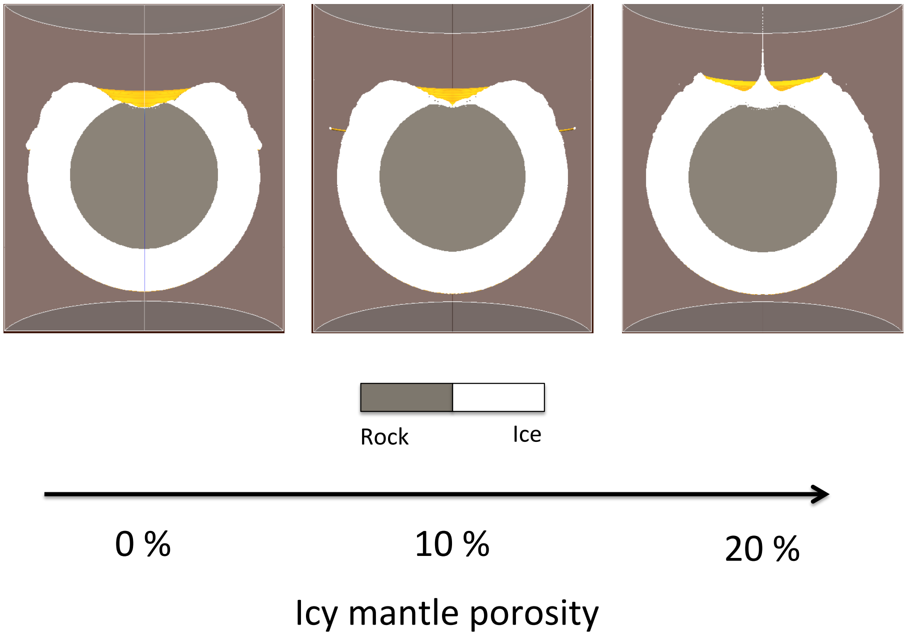

Figure 4: Material repartition as a function of the icy mantle porosity one hour after the impact ($v_{imp} = 10v_{esc}$, $R_{imp} = 25$ km). The rocky core is represented in grey while the icy material is represented in white. In these models, the grid resolution is 1 km in all directions.

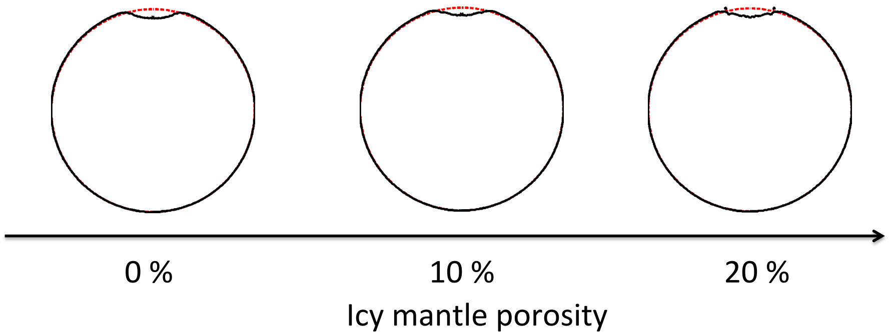

Figure 5: Rocky core morphology as a function of the icy mantle porosity (with $R_{core} = 160$ km). For each morphology, the red circle represents the pre-impact spherical shape of the impacted core.

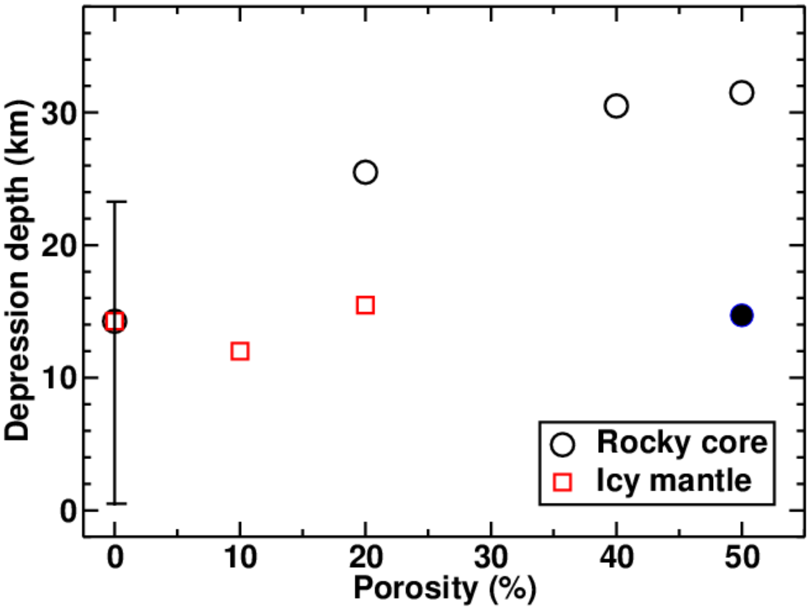

Figure 6: Depth of the impact induced depression as a function of the rocky core porosity (black circles) and as a function of the icy mantle porosity (red squares) ($v_{imp} = 10 v_{esc}$ and $R_{imp} = 25$ km). The vertical line for 0% porosity represents the range of depression depths obtained when considering a 100% icy (lower value) and a 100% rocky (upper value) impactor. The black filled circle at 50% porosity represents the unrealistic case with a core radius of 160 km (while in the other cases the core radius increases with porosity).

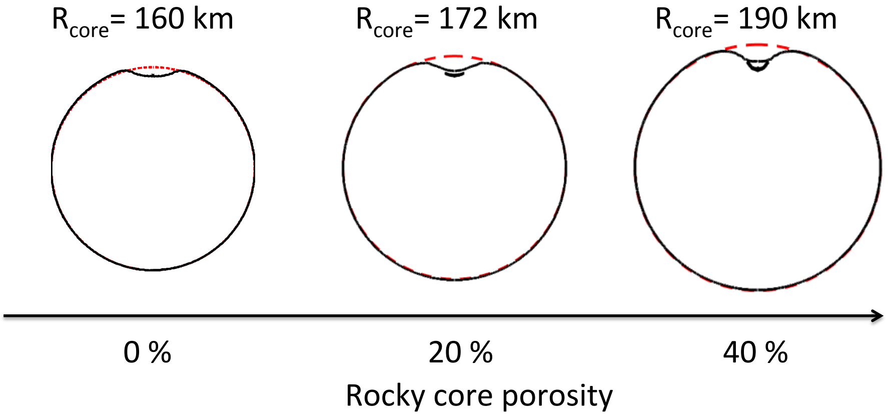

Figure 7: Rocky core morphology as a function of the rocky core porosity. For each morphology, the red circle represents the pre-impact spherical shape of the impacted core.

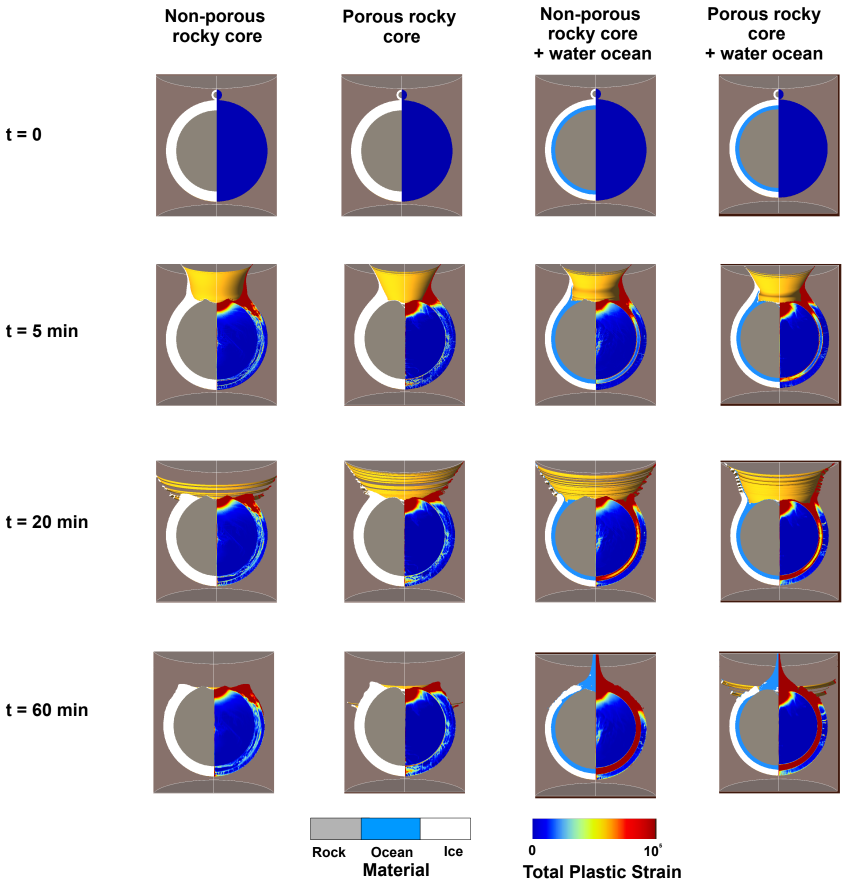

Figure 8: Material repartition (left column) and total plastic deformation (right column) as a function of time (from top to bottom) on Enceladus for $R_{core} = 200$ km, ($v_{imp} = 10 v_{esc}$ and $R_{imp} = 25$ km). We consider 4 models: a non-consistent non-porous rocky core (first column), a porous rocky core with a porosity of 50 % (second column), a non-consistent non-porous rocky core overlaid by a 20 km thick water ocean (third column) and a porous rocky core with a porosity of 50 % overlaid by a 20 km thick water ocean (fourth column). In these models, the grid resolution is 1 km in all directions.

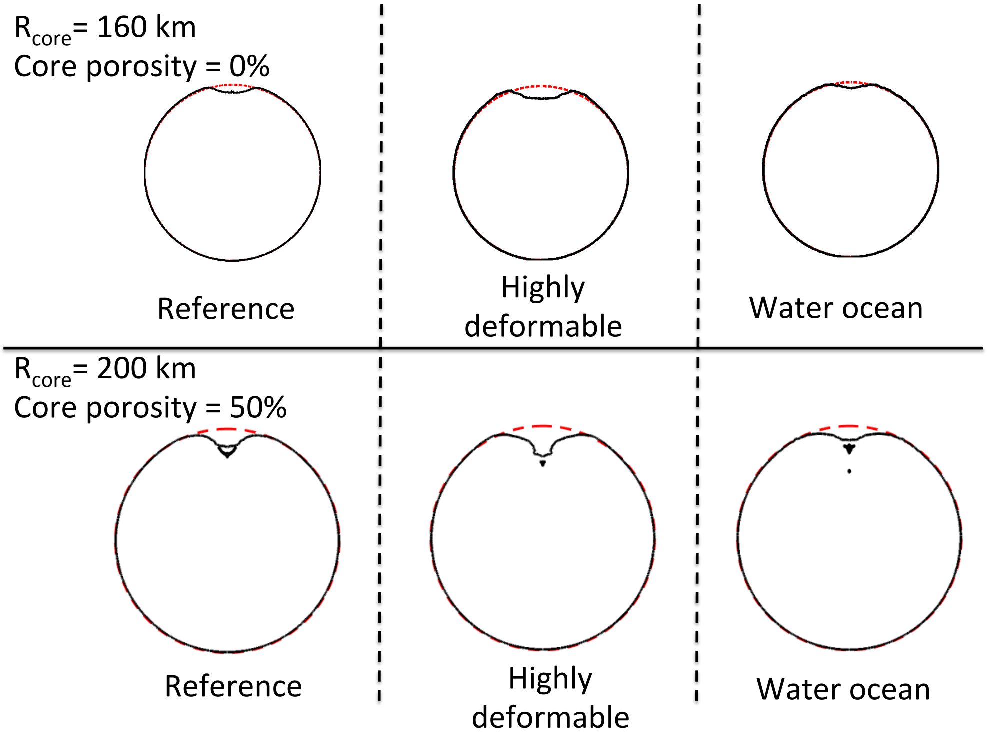

Figure 9: Rocky core morphology for different pre-impact core radii (R_{core} = 160 km (top) and 200 km (bottom)). First and third columns: Y_i = 500 kPa and Y_s = 10 MPa, second column ("highly deformable") Y_i = 10 kPa and Y_s = 100 kPa. In the third column we consider a water ocean (with a thickness of 20 km) above the rocky core. For each morphology, the red circle represents the pre-impact spherical shape of the impacted core.